Inelastic electron scattering from ^{18}O

B. E. Norum,* M. V. Hynes,† H. Miska,‡ W. Bertozzi,
J. Kelly, S. Kowalski, F. N. Rad,§ C. P. Sargent,
T. Sasanuma,|| and W. Turchinetz
Department of Physics and Laboratory for Nuclear Science, Massachusetts Institute of Technology, Cambridge, Massachusetts 02139

B. L. Berman
Lawrence Livermore Laboratory, University of California, Livermore, California 94550
(Received 4 December 1981)

Inelastic electron scattering from the low-lying even-parity states of ^{18}O has been performed. The measurements span a range in momentum transfer from 0.6 to 2.7 fm^{-1}. Form factors have been determined for the two lowest 0^+ excitations, the three lowest 2^+ excitations, and the three lowest 4^+ excitations. Transition densities for the 2^+ and 4^+ excitations have been obtained from a Fourier-Bessel analysis of these data. Comparisons were made with the predictions of various theoretical calculations and the agreement was found generally to be poor. A coexistence model was used to decompose the measured form factors into their single-particle and collective components, which in turn were compared with their counterparts in ^{16}O and ^{17}O. The results indicate that this model provides a useful framework within which to understand the structure of the oxygen isotopes. Transition densities also were obtained within the context of this model.

[NUCLEAR REACTIONS $^{18}O(e,e')$ low-lying even-parity excited states; measured form factors at 90° and 160°, $0.6 \leq q \leq 2.7$ fm^{-1}; comparison to shell and coexistence models; transition densities extracted.]

I. INTRODUCTION

The structure of the low-lying, even-parity states in the oxygen isotopes has long been a problem in nuclear physics. In the simple shell model of ^{16}O, even-parity excitations require the promotion of either one particle from the $0p$ shell to the $1p\,0f$ shell or two particles from the $0p$ shell to the $1s\,0d$ shell. The energy involved is of the order to $2\hbar\omega$ or about 30 MeV, in sharp contrast to the actual excitation energies of the lowest 0^+ (6.05 MeV) and 2^+ (6.92 MeV) states in ^{16}O. In the simple shell model of ^{18}O, two neutrons in the $1s\,0d$ shell are bound to an inert ^{16}O core. By rearranging the valence neutrons within this shell and coupling them to different angular momenta J, one can construct ten states with even values of J; three 0^+ states, five 2^+ states, and two 4^+ states. Many shell-model calculations have been performed using this basis.[1–5] This picture clearly is too simple. The electromagnetic transitions between low-lying states are greatly enhanced over what would be expected for neutron transitions. This suggests that the ^{16}O core is playing a large role in these excitations.

Brown[6] provided the basis for much of the subsequent theoretical work when he suggested that admixtures of states of permanent deformation coexist with the standard shell-model states in the low-lying levels of these isotopes. The structure of these deformed states remains an open question, although several descriptions have been attempted.[7–12] An alternative approach to the problem is simply to expand the shell-model basis by including the $0p_{1/2}$ shell; in the case of ^{18}O, by allowing four-particle, two-hole (4p2h) contributions to mix with the standard 2p0h configurations.[13,14] The energy level spectra calculated in several of these references are shown in Fig. 1.

Much information about the structure of ^{18}O exists in addition to the transition rates mentioned above; a complete compilation can be found in Ref. 15. Two previous inelastic electron-scattering experiments on ^{18}O are described in the literature.[16,17] Neither of these experiments was precise enough or complete enough to yield detailed information about the wave functions involved; the present measurements, however, are precise enough and span a range in momentum transfer broad enough

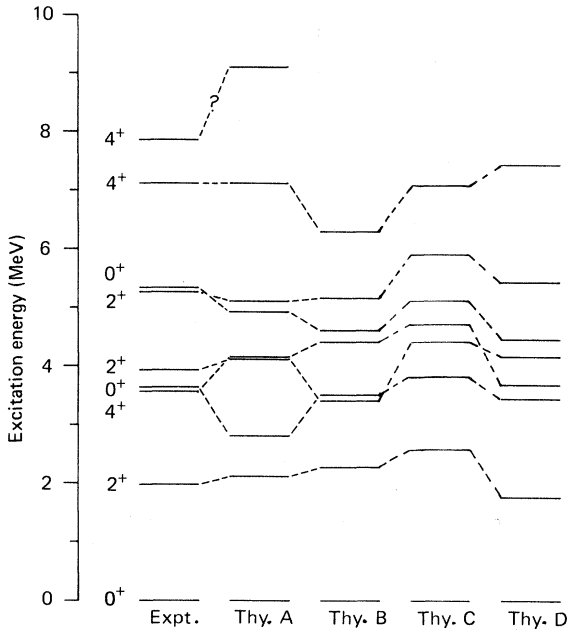

FIG. 1. Low-lying even-parity states of ^{18}O. Column 1 shows the experimentally observed spectrum. Column 2 (Thy. A) is taken from Morrison *et al.* (Ref. 12); the question mark denotes a tentative identification. Columns 3–5 (Thys. B–D) are taken from the works of Benson and Irvine (Ref. 10), McGrory and Wildenthal (Ref. 14), and Ellis and Engeland (Ref. 13), respectively.

to provide this information.

Perhaps the most interesting possibility posed by this experiment is the prospect of performing detailed comparisons between the results obtained for ^{18}O and the corresponding results for ^{16}O and ^{17}O. This has been done for elastic electron[18] and proton[19] scattering from these isotopes, and the extension to inelastic scattering promises to be even more fruitful.[20]

The scope of this paper is restricted to the low-lying even-parity, even-spin states in ^{18}O. These include the two 0^+ excitations at 3.62 and 5.33 MeV, the three 2^+ excitations at 1.98, 3.92, and 5.25 MeV, and the three 4^+ excitations at 3.55, 7.11, and 7.85 MeV, shown in the Expt. column of Fig. 1. Simultaneous measurements of the form factors of the first 2^+ state (6.92 MeV) in ^{16}O and the first $\frac{1}{2}^+$ state (0.87 MeV) in ^{17}O provide the bases for the comparisons alluded to above.

II. ELECTRON SCATTERING

Following Ref. 21, the plane-wave Born approximation (PWBA) cross section for the electroexcitation of a nucleus from a state of angular momentum 0^+ to a state of even angular momentum J^+ is

$$\frac{d\sigma}{d\Omega}=Z^2\sigma_M\eta\{\,|F_J^L(q)|^2 + [\tfrac{1}{2}+\tan^2(\tfrac{1}{2}\theta)]\,|F_J^T(q)|^2\}\,, \quad (1)$$

where Z is the atomic number of the target nucleus,

$$\sigma_M=(\alpha/2E_0)^2\cos^2(\tfrac{1}{2}\theta)/\sin^4(\tfrac{1}{2}\theta)$$

is the Mott cross section, α is the fine-structure constant, E_0 is the incident electron energy, θ is the scattering angle,

$$\eta=[1+(2E_0/M)\sin^2(\tfrac{1}{2}\theta)]^{-1}$$

is the recoil factor, M is the mass of the target nucleus, $F_J^L(q)$ is the longitudinal (or Coulomb) form factor, and $F_J^T(q)$ is the transverse electric form factor. The three-momentum transfer q is given by

$$q\approx 2E_0\eta^{1/2}\sin(\tfrac{1}{2}\theta)(1-\omega/E_0)^{1/2}\,, \quad (2)$$

where ω is the energy to which the nucleus is excited. The form factors F_J^L and F_J^T can be written in terms of the electromagnetic transition operators (M_J^C, T_J^E) as

$$|F_J^L(q)|^2=\frac{4\pi}{Z^2}\,|\langle J||M_J^C(q)||0\rangle|^2\,,$$

$$|F_J^T(q)|^2=\frac{4\pi}{Z^2}\,|\langle J||T_J^E(q)||0\rangle|^2\,. \quad (3)$$

The longitudinal form factor $F_J^L(q)$ is related (in PWBA) to the transition charge density $\rho_{\rm tr}^J(r)$ by

$$\rho_{\rm tr}^J(r)=\int F_J^L(q)e^{i\vec{q}\cdot\vec{r}}d^3q\,.$$

The transition charge density is in turn related to the corresponding multipole moment by

$$\sqrt{B(EL)}=\left[\frac{2J_f+1}{2J_i+1}\right]^{1/2}\int\rho_{\rm tr}^L(r)r^{L+2}dr\,,$$

where J_i (J_f) is the spin of the initial (final) state.

The preceding equations (1)–(3) do not take account of the distortion of the electron waves by the Coulomb field of the nucleus. A precise, although still approximate, method of dealing with Coulomb effects is the distorted-wave Born approximation (DWBA). In DWBA, the electron-nucleus interaction still is treated in lowest-order perturbation theory, but the electron waves are no longer plane waves. Rather, they are solutions of the Dirac equation in the presence of the spherically symmetric part of the ground-state charge distribution.

To first order, the effect of the distortion of the electron waves is to increase the momentum transfer which characterizes the nuclear scattering event. The relation between the momentum transfer q, as calculated from the kinematics of the scattering event to the effective momentum transfer q_{eff}, which represents better the momentum actually transferred during the scattering event, is[22]

$$q_{\text{eff}} = 1\left[1+\frac{3}{2}\left[\frac{3}{5}\right]^{1/2}\frac{Z}{E_0\langle r^2\rangle^{1/2}}\right],$$

where $\langle r^2\rangle^{1/2}$ is the root-mean-square (rms) radius of the nuclear charge distribution. For most facets of the present work this correction for Coulomb effects would have been adequate. However, in most cases full DWBA calculations were performed.

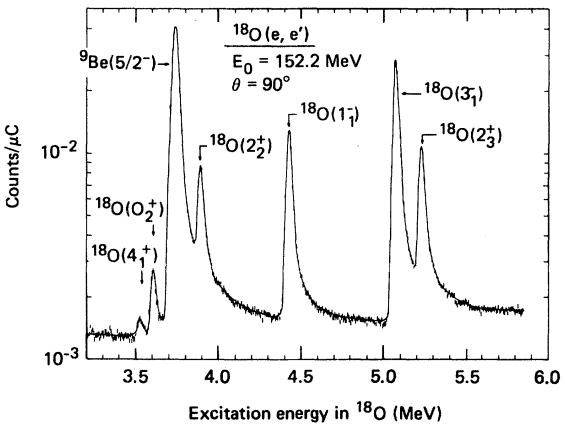

FIG. 2. Spectrum of electrons with incident energy 152.2 MeV scattered at 90° from an isotopically enriched (^{16}O—7%, ^{17}O—2%, ^{18}O—91%) beryllium-oxide foil. The leftmost two peaks are separated by only 80 keV. The solid curve represents a least-squares fit to the data.

III. EXPERIMENT AND DATA REDUCTION

A. Experimental details

The present experiment was performed at the MIT-Bates linear accelerator[23,24] using the high-resolution MIT energy-loss spectrometer.[25] Figure 2 shows a representative scattered-electron spectrum measured during this experiment. The leftmost two peaks [^{18}O (4_1^+) and ^{18}O (0_2^+)] are separated by 80 keV and are seen to be resolved clearly.

The measurements comprising this experiment were made at scattering angles of 90° and 160°. For the measurements made at 90°, incident electron energies between 90 and 370 MeV were used to obtain a range in momentum transfer from 0.6 to 2.7 fm^{-1}. Energies between 125 and 275 MeV were used for the 160° measurements, corresponding to a range in momentum transfer from 1.3 to 2.7 fm^{-1}.

The targets used in this experiment were beryllium-oxide foils enriched to varying degrees in ^{17}O and ^{18}O. They were fabricated at the Lawrence Livermore Laboratory using novel chemical and metallurgical techniques.[26] First, water containing isotopically enriched oxygen was vaporized and allowed to react with gaseous beryllium chloride, yielding a solution of BeO and HCl. Ammonia then was introduced, reacting with the HCl to cause the BeO to form a white powdery precipitate. These reactions are very selective and thereby ensured that all of the beryllium and oxygen in the precipitate was in the form of BeO. The BeO was pressed and sintered into thick wafers, which were lapped down to the final thicknesses. The thicknesses of the five targets ranged from 21 to 47 mg/cm^2 (see Table I).

Electrons scattered elastically from nuclei with different masses have final energies which are separated by the differential kinematic recoils of the nuclei. The high resolution of the MIT energy-loss spectrometer enabled us to separate the oxygen elastic peaks at all energies used in the present experiment. Figure 3 shows the elastic region of a typical

TABLE I. Target compositions.

Target	Thickness (mg/cm^3)	Isotopic abundance ^{16}O (%)	^{17}O (%)	^{18}O (%)
Be^{18}O	47.2	7.2±0.1	2.0±0.1	90.8±0.4
Be^{16,18}O	45.8	55.8±0.6	1.0±0.1	43.2±0.5
Be^{16,18}O	21.6	52.3±0.4	1.0±0.1	46.7±0.5
Be^{16,17,18}O	42.5	14.1±0.3	19.7±0.4	66.2±0.1
Be^{16,17,18}O	21.3	14.2±0.1	19.2±0.4	66.7±0.4

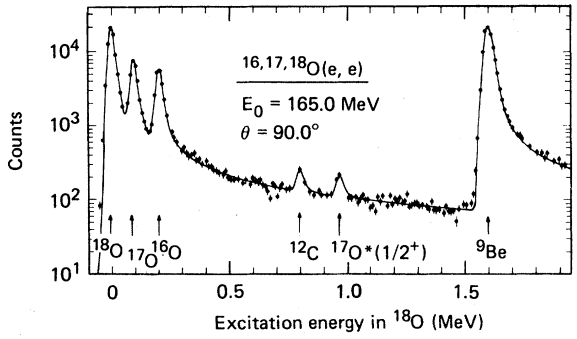

FIG. 3. Spectrum of electrons with incident energy 165.0 MeV scattered at 90° from an isotopically mixed (^{16}O—14%, ^{17}O—19%, ^{18}O—67%) beryllium-oxide foil. The clearly resolved peaks corresponding to elastic scattering from the three oxygen isotopes are separated by their different recoil energies.

spectrum. In addition to the elastic peaks of beryllium and the three oxygen isotopes, one can see that of the small carbon impurity in the target.

The relative abundances of the oxygen isotopes were determined by comparing elastic-scattering data from our set of enriched-isotope targets with data obtained from a BeO target in which the oxygen isotopes are present in their natural abundances (see Appendix B). The results are listed in Table I.

B. Data reduction and error analysis

The present work comprises one facet of a wider study of electron scattering from the three stable oxygen isotopes; further details can be found in Refs. 18, 27, and 28.

High-quality absolute measurements of elastic electron scattering from ^{16}O have been made elsewhere.[29,30] A reanalysis of these data[18] yielded an accurate parametrization of the ^{16}O ground state charge distribution (see Appendix C). Measurements of elastic scattering from ^{18}O made using targets containing both ^{16}O and ^{18}O were normalized to the ^{16}O elastic cross sections computed from this distribution. From these measurements a parametrization of the ^{18}O ground state was extracted that is almost as precise as that of the charge distribution of ^{16}O (see Appendix C). The inelastic cross sections were normalized to the elastic cross sections of both ^{16}O and ^{18}O as measured during the same exposure. This made them independent of (1) dead-time corrections, (2) beam-current monitoring, (3) fluctuations in target thicknesses, and (4) uncertainty in the spectrometer acceptance.

The energy scale of the focal-plane detectors was calibrated using the energy spacings between peaks corresponding to excited states of the nuclei present in the mixed-isotope targets; the incident energy E_0 was determined using the separations (due to differential recoil energy loss) between peaks corresponding to states in different nuclei. The precision of this calibration typically was of the order of 5 to 10×10^{-4} ($\Delta E_0/E_0$).

Corrections of the scattered-electron spectra for dead-time losses were not necessary because only ratios were required. However, it was important that the dead-time effects be uniform across the focal plane. This requirement was tested by measuring an ^{18}O spectrum twice, once with a low counting rate and once with a high rate. From each spectrum the ratio of the cross sections for the ground state and the first excited state (1.982 MeV) was extracted. The two measurements were compared and were found to agree within the statistical limits ($<1\%$).

There were a few locations in the focal plane detectors near which the energy of detected electrons was sometimes misidentified. No valid events were lost thereby, but apparent $5-10\%$ fluctuations in detection efficiency resulted. The errors in energy identification were very small so the inefficiencies were very localized compared to the widths of the peaks in the spectra. These regions of the focal plane were either avoided or rendered unimportant by averaging spectra obtained using several focal plane positions. Line shape fitting of the spectra further reduced the impact of these fluctuations by effectively averaging the data from many channels. The net uncertainty introduced by these fluctuations was within $\pm1\%$.

Peak areas and corresponding cross sections were extracted from the composite spectra using a least-squares fitting technique based upon the routine CURFIT.[31] The fitting function used consisted of a polynomial background plus an arbitrary number of peaks. The natural widths of the states of interest in this work are narrow, the widest being about 3 keV. Thus, the shapes of the peaks in the spectra were determined by the system resolution function and the radiative tails. The peak shapes used in the present analysis were computed using the procedure developed by Bergstrom,[32] in which the total peak shape is formed by convoluting a system resolution function with a radiative-response function that describes the peak shape which would result if the incident beam energy profile were a delta function. The calculations of radiative processes were performed in PWBA, neglecting recoil effects. This has been estimated to introduce an error of not

more than one percent, although in most cases even this error was common to both elastic and inelastic peaks and hence was cancelled out.

The independence from systematic effects leaves the fitting step as the major source of uncertainty in the extracted cross sections. The uncertainty in each peak area was estimated in two ways. First, the number of counts assigned to a peak was used to compute a statistical error estimate. Second, the uncertainty in each parameter used to define a peak was determined using the procedure outlined in Ref. 31. The resulting uncertainty in the peak area was computed by adding in quadrature the changes in the area generated by increasing each parameter by its corresponding uncertainty. The larger of these two estimates was accepted.

The uncertainty in the normalization resulting from the uncertainty in the computed ^{16}O and ^{18}O elastic cross sections ranges from 0.2% at 50 MeV to about 10–15% in the elastic diffraction minimum and above an incident energy of 350 MeV.

The uncertainty in the normalization resulting from an uncertainty ΔE_0 in the incident energy E_0 is of the order of 2%, except near the diffraction minimum of the elastic scattering where it rises to about 5%.

The uncertainty in the average scattering angle θ is less than 0.05° (1 mr). For the measurements reported here the horizontal (scattering plane) angular acceptance of the spectrometer was 26 mrad; the vertical acceptance was 121 mrad. The resulting fractional uncertainty in the average momentum transfer is at most 5×10^{-4}, and generates uncertainties in the cross sections of 0.3–0.5%.

The uncertainties in the relative abundances of the oxygen isotopes in the targets are negligible (see Table I). Furthermore, a weighted average of the ^{16}O and ^{18}O elastic cross sections was used to normalize the inelastic ^{18}O data. Any error in the abundance of ^{18}O would imply an error of opposite sign in the abundances of the other isotopes. These errors tended to cancel when the elastic cross sections of both ^{16}O and ^{18}O were used to normalize the inelastic data.

IV. RESULTS AND DISCUSSION

A. Measured form factors

The form factors of the low-lying, even-parity states of ^{18}O measured in this experiment are shown in Figs. 4–10 and are tabulated in Appendix A. In these figures

$$|F|^2=(d\sigma/d\Omega)/Z^2\sigma_M\eta\ .$$

Figure 4 shows the form factors, measured at 90°, of the first two excited 0^+ states (0_2^+,0_3^+). The form factor of the 0_2^+ state is seen to be well sampled throughout the momentum-transfer region from 0.6 to 2.7 fm^{-1}, while the paucity of data on the 0_3^+ state reflects the extreme weakness of its coupling to the ground state. A previous measurement[17] indicated that the form factor of the 0_3^+ state reaches 5×10^{-4} at a momentum transfer of about 1 fm^{-1}. The absence of any visible structure near 5.33 MeV excitation in Fig. 2 implies that the form factor of this state cannot exceed 4 or 5×10^{-5}.

Figures 5–7 show the form factors of the first three 2^+ states (1.982, 3.919, and 5.250 MeV), measured at 90°. The form factor of each is seen to be clearly defined throughout the momentum-transfer range from 0.6 to 2.7 fm^{-1}. In particular, the locations of the diffraction minima are well defined (see Table III). In cases where a minimum in a form factor results from cancellations of competing amplitudes, these locations can provide sensitive

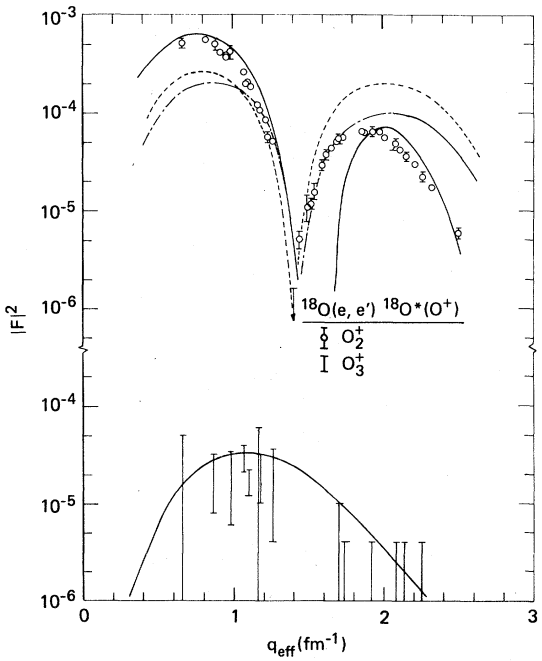

FIG. 4. Form factors for the lowest two 0^+ excitations in ^{18}O, measured at 90° (data points). The solid and dashed curves are from Refs. 33 and 34, respectively. The dotted-dashed curve was computed from wave functions given in Ref. 10.

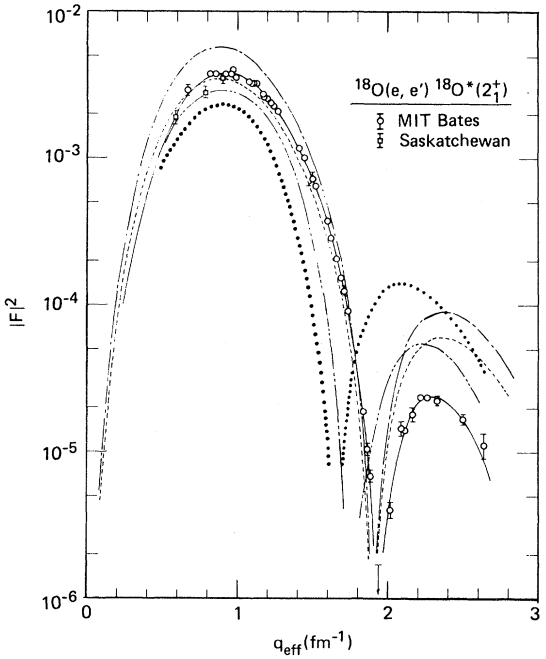

FIG. 5. Measured form factors for the lowest 2^+ excitation in ^{18}O. The circles represent our measurements made at 90°; the squares are taken from Ref. 17. The solid curve shows the result of an FBA fit to the data. The dashed (dashed-dotted) curve was computed using wave functions from Ref. 14 and $e_{pol}=0.33e$ ($e_{pol}=0.50e$). The dashed-dotted-dotted curve is taken from Ref. 34, while the dotted curve was computed using wave functions from Ref. 10.

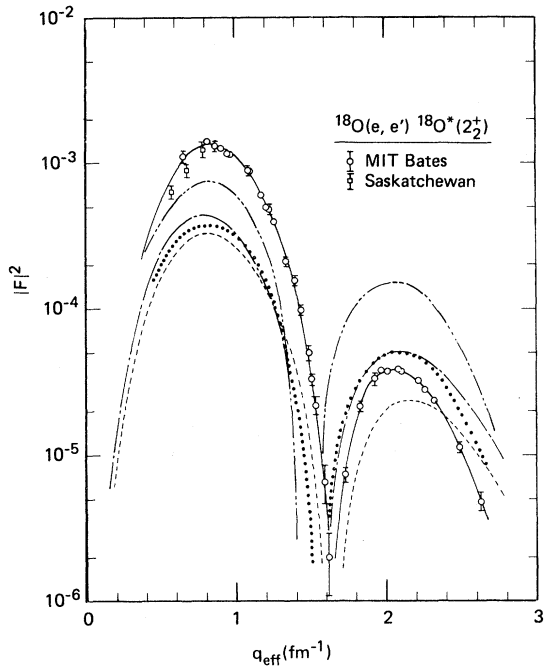

FIG. 6. Measured form factors for the second 2^+ excitation in ^{18}O. See caption for Fig. 5 for description of points and curves.

measures of the mixing of those amplitudes.

The 90° measurements of the form factors of the lowest three 4^+ states (3.553, 7.114, and 7.848 MeV) are presented in Fig. 8. The identification of the 7.848-MeV level as the third 4^+ state is not definite; a spin assignment of $J=4\pm1$ was made by Fortune *et al.*[35] on the basis of total cross-section measurements of the $^{13}C(^6Li,p)$ reaction. Arguments presented below show that our data lend credence to the 4^+ assignment.

Figures 9 and 10 show the results of the 160° measurements. The 0_3^+ peak was not discernible at 160°, and the 7.848-MeV peak either did not fall on the detectors (at low incident energies) or was occluded by the many nearby peaks (at higher energies). For the measurements at 160° only targets containing appreciable amounts of ^{17}O were used (see Table I). The resulting high density of peaks above 7 MeV made the extraction of reliable cross sections for the 7.848-MeV level impossible. It was possible, however, to establish upper limits on the cross sections. By establishing the upper limits on

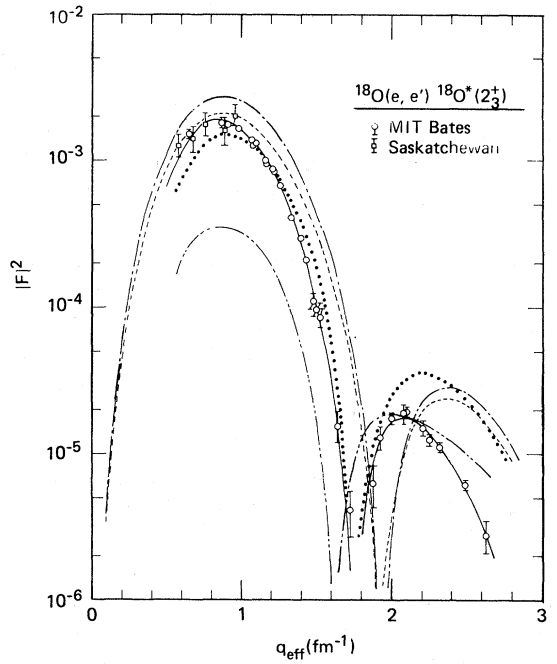

FIG. 7. Measured form factors for the third 2^+ excitation ^{18}O. See caption for Fig. 5 for descriptions of points and curves.

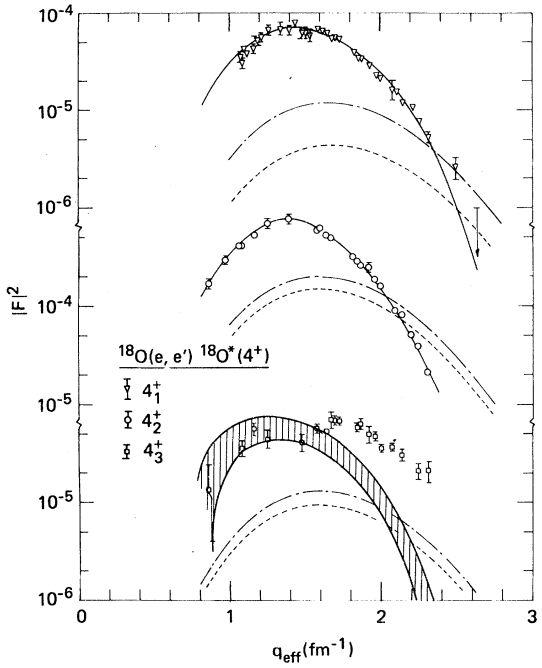

FIG. 8. Measured form factors for the lowest three 4^+ states in ^{18}O. The data points represent our measurements made at 90°. See caption for Fig. 5 for descriptions of curves. The shaded band represents the form factor for the third 4^+ state computed [within the context of the LSF (Ref. 11) model] from those measured for the lowest two 4^+ states.

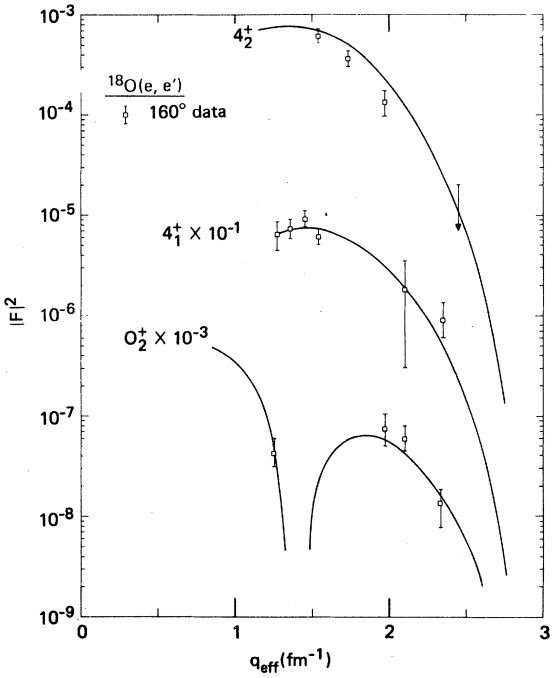

FIG. 9. Form factors for the lowest 0^+ excitation and the two lowest 4^+ excitations in ^{18}O, measured at 160°. The solid curves are computed from the measurements made at 90° under the assumption that the transitions are purely longitudinal.

the total form factors $|F|^2$ measured at $\theta=160°$ to be similar to those measured at $\theta=90°$ it was concluded that the transverse form factor of the 7.848-MeV excitation cannot exceed $\frac{1}{10}$ the longitudinal form factor.

The curves that pass through the form factors of the 2^+ and 4^+ states in Figs. 9 and 10 were generated (using DWBA) from Fourier-Bessel analyses[36] (FBA, see Sec. VI B) of the form factors of these states as measured at 90°. These curves represent the form factors one expects to measure at 160° if the form factors measured at 90° contain no transverse components aside from negligibly small contributions from the currents demanded by the continuity equation.[36] The curve through the form factor of the 0^+ state is a curve drawn by eye through the data measured at 90°. In spite of the relatively large errors it is evident that the form factors of these states have no significant transverse components. The absence of transverse contributions to the monopole transitions is required in order to conserve angular momentum. Transverse contributions to the 2^+ and 4^+ transitions are not forbidden, but one can understand qualitatively why they should be very small. The low-lying states in ^{18}O are dominated by two-neutron configurations. A Coulomb transition between two such states results from core-polarization effects since the neutrons themselves carry no charge. These core polarizations are collective phenomena and, accordingly, have essentially no transverse components.

B. Fourier-Bessel analysis and transition charge densities

In PWBA the form factor is related to the charge density by

$$F_J^L(q)=\frac{1}{4\pi}\int e^{-i\vec{q}\cdot\vec{r}}\rho^J(r)d^3r\ ,$$

where ρ^J is the nuclear charge distribution. For elastic scattering $\rho^J(r)$ is the ground-state distribution, while for inelastic scattering it is the transition charge density. Inverting the above equation yields

$$\rho^J(r)=\int F_J^L(q)e^{i\vec{q}\cdot\vec{r}}d^3q\ .$$

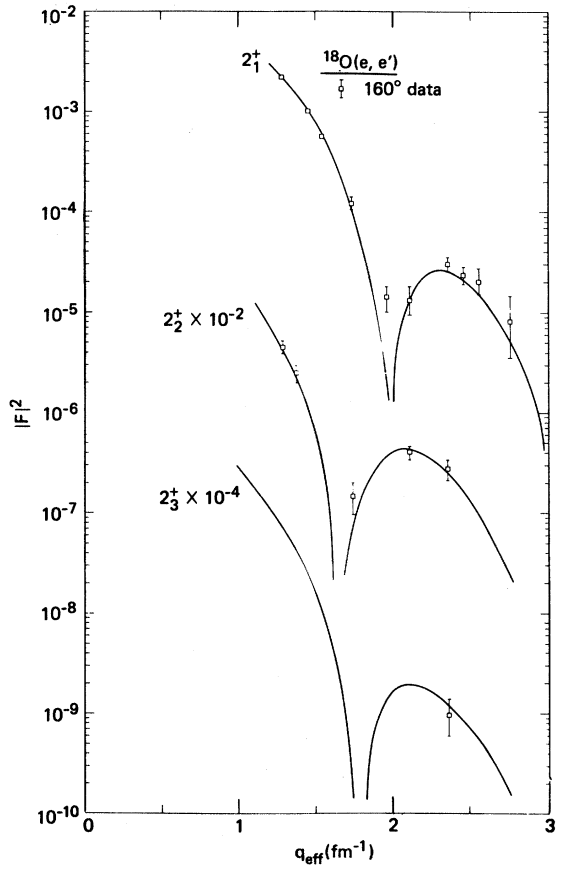

FIG. 10. Form factors for the lowest three 2^+ states in ^{18}O as measured at 160°. The solid curves are computed from the measurements made at 90° under the assumption that the transitions are purely longitudinal.

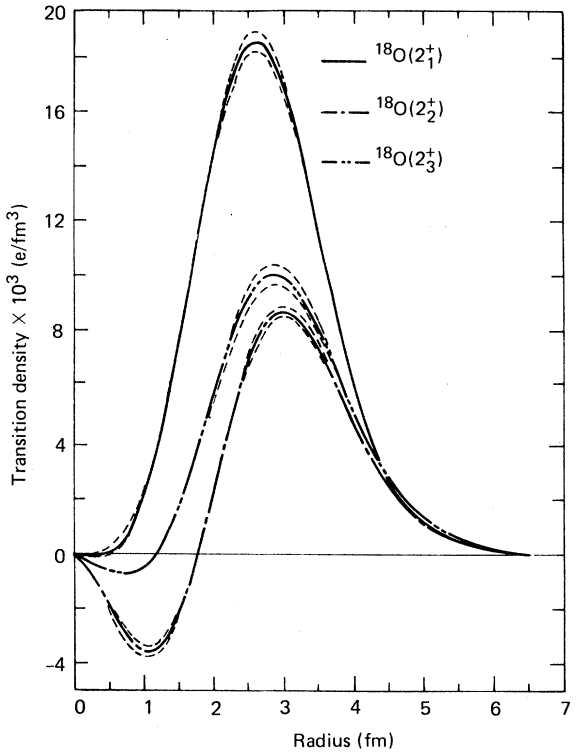

FIG. 11. Transition charge densities for the lowest three 2^+ states in ^{18}O (2_1^+-1.982 MeV, 2_2^+-3.919 MeV, 2_3^+-5.250 MeV) as determined from the measurements made at 90°.

Two different parametrizations $\rho(r)$ were used in the present work. First, the elastic scattering from ^{16}O and ^{18}O, as well as the pseudoelastic (see Sec. IV D) scattering from ^{18}O, were analyzed following the method of Friar and Negele.[37] In this approach the ground-state distribution is described by

$$\rho(r)=\rho_0(r)+\Delta\rho(r)$$
$$=\rho_0(r)+\sum_{n=1}^{N}\frac{C_n}{r}\sin\left[\frac{n\pi r}{R}\right]\theta(R-r)\ ,$$

where $\rho_0(r)$ is an initial estimate of $\rho(r)$ and $\Delta\rho(r)$ is determined by the parameters C_n which are adjusted to fit the data. The parameter R is the radius beyond which $\rho(r)$ is described sufficiently well by $\rho_0(r)$. The application of this technique to the elastic scattering from the oxygen isotopes is given in Ref. 18.

The inelastic data (2^+ and 4^+ only) were analyzed following the method of Heisenberg.[36] In this approach the 2^J-pole transition density is described by

$$\rho_{tr}^J(r)=\sum_{n=1}^{N}a_n X_n^{J-1} j_J(X_n^{J-1}r/R)\theta(R-r)\ ,$$

where X_n^{J-1} is the nth zero of the spherical Bessel function $j_{J-1}(x)$. Here, R is the radius beyond which the transition density is assumed to be zero.

The measurements made at 90° for each of the three 2^+ states and the lowest two 4^+ states were subjected to FBA; the solid curves in Figs. 5–8 show the fitted form factors obtained. The quality of the fits is seen to be very good (the reduced χ^2 for the five fits range from 0.8 for the 2_1^+ state to 1.6 for the 4_1^+ state). The extracted transition charge densities are shown in Figs. 11 and 12. The error envelopes on these graphs reflect both the statistical uncertainties and the incompleteness error which results from the fact that our measurements span a finite range in momentum transfer.

Figure 11 shows the transition densities for the

2^+ states. The density for the 2_1^+ state is everywhere positive while those for the 2_2^+ and 2_3^+ states are negative near the origin. For nuclei in the oxygen region, the participation of an s orbital is required in order to generate a lobe in the transition density so deep inside the nucleus. Therefore, it is clear that the 0_1^+ to 2_1^+ transition is dominated by d-to-d transitions, while the other two contain appreciable d-to-s (or s-to-d) components. The expansion parameters for these transition densities are given in Appendix D.

Figure 12 shows the transition densities for the hexadecapole transitions. They are seen to be very similar in shape. This is not surprising since the major contributor to $L=4$ transitions is the d-to-d transition. To generate another 4^+ transition one must either promote a particle from the $0p$ shell to the $0f$ shell or start with two particles in the $1p0f$ shell and recouple them to $J=4$. Energetic considerations lead one to expect that such contributions to the low-lying states of ^{18}O are small. The expansion parameters for these transition densities are given in Appendix D.

The reduced transition probabilities [$B(EL)$'s] extracted from the FBA fits to the 2^+ and 4^+ cross sections are shown in Table II. It should be noted that the data used in these analyses comes from measurements made at momentum transfers above 0.6 fm^{-1}, a region from which extrapolation to the photon point is not a model-independent procedure. Nonetheless, the value obtained for the transition to the 2_1^+ state is in excellent agreement with recent measurements; Flaum *et al.*[38] report a value of 45.3 ± 2.5 e^2fm^4 and Vold *et al.*[39] report 40.2 ± 1.2 e^2fm^4.

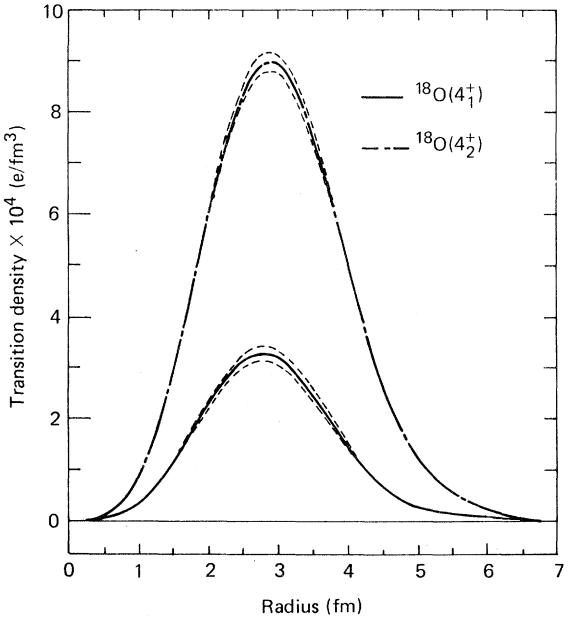

FIG. 12. Transition charge densities for the lowest two 4^+ states in ^{18}O (4_1^+-3.553 MeV, 4_2^+-7.114 MeV) as determined from the measurements made at 90°.

TABLE II. Reduced transition probabilities.

State	$B(EL;\ 0_1^+\rightarrow L^+)$ (e^2fm^{2L})
2_1^+ (1.982 MeV)	44.8 ± 1.3
2_2^+ (3.919 MeV)	22.2 ± 1.0
2_3^+ (5.250 MeV)	28.3 ± 1.5
4_1^+ (3.553 MeV)	$(9.04\pm0.90)\times10^2$
4_2^+ (7.114 MeV)	$(1.31\pm0.06)\times10^4$

C. Comparisons with theoretical calculations

Most of the theoretical work done on ^{18}O falls into one of two categories. First, there are the extended-basis shell-model calculations containing 2p0h and 4p2h configurations with respect to a closed $0p$ shell. The subshells available to the particles and holes vary, as do the residual two-body interactions. In the calculation of McGrory and Wildenthal,[14] which is based upon the earlier work of Zuker *et al.*,[40] the basis is truncated to include only the $0p_{1/2}$, $0d_{5/2}$, and $1s_{1/2}$ orbitals. Another approach is that of Ellis and Engeland[13] in which allowed configurations are chosen using more physical criteria, such as energetics. The second category is composed of the coexistence models, in which 2p0h shell-model states are combined with one or more strongly deformed states. Representative of this genre are the works of Benson and Irvine,[10] Morrison *et al.*,[12] and Lawson *et al.*[11]

None of these models can tell the complete story. The hope, of course, is that they can help in identifying which degrees of freedom in the nucleus play major roles in determining its properties. It is possible, in some cases, to reproduce simultaneously $B(EL)$ values and static moments by assigning "effective" or "polarization" charges to the nucleons active in the model. These polarization charges clearly are only a convenient means of parametrizing the polarizing effects of the valence nucleons on the core; thus, they represent the degree to which polarizations of the rest of the nucleus influence the

transitions. Within the context of the shell model, these polarizations take the form of particle-hole excitations that fall outside the basis used in the structure calculations. The question of whether the polarization charges are independent of momentum transfer and therefore useful when discussing electron scattering has been addressed by Horsfjord.[33] His work suggests that in the case of the oxygen isotopes constant polarization charges are useful up to a momentum transfer of approximately 2 fm^{-1}. Therefore, comparisons of the calculations to the data beyond the first diffraction minima should be trreated with extreme caution.

In order to compare the point nucleon form factors computed from the shell model wave functions to experimental data one must account for (a) the finite charge distribution of the proton and (b) the lack of translational invariance of the shell model wave functions. The former can be dealt with by multiplying the point nucleon form factors by the proton form factor [$F_p(q)$] which, for the range of momentum transfer of interest here, is adequately described by the dipole approximation[21]

$$F_p(q)=(1+q^2/18.774\ \text{fm}^{-2})^{-2}\ .$$

The latter can be accounted for approximately by multiplying the point nucleon form factors by $F_R(q)$, the "recoil correcton" factor

$$F_R(q)=e^{q^2b^2/2A}\ ,$$

where b is the oscillator length parameter of the well that best describes the nuclear potential, and A is the mass number.

The magnitudes of the above corrections are not trivial; at a momentum transfer of 2 fm^{-1}, for instance, F_p is about 0.5 and F_R ($b=1.8$ fm, $A=18$) is about 1.4. Combined, they produce a 30% effect.

The calculation of McGrory and Wildenthal[14] was performed using a basis spanned by the $0p_{1/2}$, $0d_{5/2}$, and $1s_{1/2}$ subshells. All 2p0h and 4p2h configurations allowed by the Pauli principle were included. The radial wave functions were computed using a Woods-Saxon potential, the parameters of which were chosen to reproduce ^{16}O and ^{17}O binding energies. The energy-level scheme predicted by this model is shown in column C of Fig. 1. It should be noted that the composition of the shell-model wave functions is much less sensitive to the details of the Hamiltonian than is the placement of the energy levels. Thus, it would not be inconsistent if the wave functions, and the form factors computed from them, gave a better description of the properties of this nucleus than is suggested by the energy-level spectrum.

When this model was used to calculate electron-scattering form factors for comparison with the present data, constant polarization charges of 0.33e and 0.50e were used. The first value was chosen to reproduce the measured[38,39] $B(E2)$ value for the 2_1^+-to-0_1^+ transition, and the second was used to obtain a measure of the sensitivity of the form factors to the choice of polarization charge. The form factor of the 2_1^+ transition correctly reproduces the location of the first minimum (see Fig. 5). However, the shortcomings of this calculation are evident from Figs. 6 and 7.

The model of Ellis and Engeland[13] differs significantly in that it is based upon the assumption that correlations between particles in the same major shell are of predominant importance. Accordingly, the 4p2h states were formed by combining eigenfunctions obtained by solving the four-particle problem in the $1s\,0d$ shell with solutions of the two-hole problem in the $0p$ shell. Horsfjord[41] repeated the Hamiltonian diagonalization treating the intrinsic energy separation E between the 2p0h and 4p2h states as a free parameter and computed (using a polarization charge of 0.5e for each nucleon) electron-scattering form factors for the 0_2^+ and 0_3^+ states as functions of E.

When a value for E of -0.9 MeV is assumed, a reasonable fit to the amplitude of the first maximum in the form factor of the 0_2^+ state is obtained (see Fig. 4). However, the location of the minimum is predicted wrongly, as is its breadth. The prediction for the form factor of the 0_3^+ state is seen to be in agreement with the limits established by the present data.

Although form factors calculated from the above model are not available for the 2^+ states, predictions of the locations of the minima are. Table III shows the locations of the minima computed using either a constant polarization charge or calculated, q-dependent polarization effects. Two different forms were used for the particle-hole interaction when the polarization effects were calculated; the

TABLE III. 2^+ diffraction minima.

	2_1^+ (fm^{-1})	2_2^+ (fm^{-1})	2_3^+ (fm^{-1})
$e_{\text{pol}}=0.5$	1.87	1.37	1.85
QQ	2.00	1.91	1.87
Y	2.11	1.27	1.92
Experiment	1.96±0.02	1.62±0.02	1.76±0.04

quadrupole (QQ) interaction of Harvey and Khanna[42] and a Yukawa (Y) interaction. No calculation is seen to be consistent with the data, although two of them ($e_{\text{pol}}=0.5e$, Y) correctly reproduce the relative ordering of the minima of the three 2^+ states.

One of the earliest calculations to include intrinsically deformed states was that of Benson and Irvine.[10] They used the standard 2p0h states from the spherical shell model plus a single intrinsically deformed state which is formed by removing two protons from the $0p_{1/2}$ orbital of the spherically-symmetric shell model and putting them together with two neutrons into the $k=\frac{1}{2}^+$ Nilsson[43] orbital. They calculated electromagnetic transition rates using harmonic-oscillator radial wave functions with a polarization charge of $0.5e$ assigned to each nucleon.

The form factor for the 2_1^+ transition computed using these wave functions is too low at the first maximum by a factor of 2 and locates the diffraction minimum almost 0.4 fm^{-1} too low (see Fig. 5); that for the 2_2^+ transition underestimates the maximum by a factor of 5 (see Fig. 6). For the 2_3^+ transition the agreement between the calculation and data is acceptable in the region of the first maximum.

On the other hand, Morrison *et al.*[12] generated wave functions using the multideterminant Hartree-Fock (HF) method with a six-determinant basis. Corresponding form factors were calculated for the 0_2^+ state and all three 2^+ states. In no case is the agreement satisfactory. The predicted minimum of the 0_2^+ form factor is well reproduced, but the amplitude is wrong by a factor of 2. The encouraging agreement in magnitude with the measured form factor for the 2_1^+ transition is mitigated by the sharp disagreement over the location of the minimum.

Thus, none of the above calculations yields an adequate description of the measured form factors; each success that a model achieves is accompanied by a corresponding failure.

D. Coexistence model of Lawson, Serduke, and Fortune

The model of Lawson, Serduke, and Fortune[11] (LSF) embodies a much more empirical approach to the description of the low-lying 0^+, 2^+, and 4^+ states of ^{18}O. In common with the two coexistence models discussed above, the physical states are constructed from a combination of collective deformed states and 2p0h states. However, in the other coexistence models the assumption is made that there exists a single intrinsically deformed state from which are projected states of various angular momenta, while in the LSF model the three collective states ($|\psi_J\rangle$; $J^\pi=0^+$, 2^+, and 4^+) are treated as separate entities. The allowed 2p0h $J=0$ configurations are $(d_{5/2})^2$ and $(s_{1/2})^2$. Similarly, the $J=2$ 2p0h configurations are $(d_{5/2})^2$, $(d_{5/2}s_{1/2})$, $(d_{5/2}d_{3/2})$, and $(d_{3/2}s_{1/2})$. The only 2p0h configurations with $J=4$ are $(d_{5/2})^2$ and $(d_{5/2}d_{3/2})$. Therefore, the basis of the 0^+ states has three components, that of the 2^+ states has five, and that of the 4^+ states has three. The matrix elements of the Hamiltonian connecting the basis states were determined by fitting known properties of the physical states to be described.

The model contains three further assumptions of consequence. First, the radial wave functions of the $0d_{5/2}$ and $0d_{3/2}$ orbitals are the same, but this radial dependence is not explicitly specified. Second, the polarization charge appropriate for a $0d_{5/2}$ neutron is equal to that for a $0d_{3/2}$ neutron. Third, and probably most restrictive, the collective states cannot be connected to the 2p0h states by a one-body operator, such as an electromagnetic transition operator.

Within this model the Coulomb matrix element for the excitation of a state can be expressed as a linear combination of matrix elements involving basis states. For the case of a monopole ($C0$) transition to the nth 0^+ state the matrix element is given by

$$\langle 0_n^+||M_0^C||0_1^+\rangle = A_n\langle (d_{5/2})^2;0||M_0^C||(d_{5/2})^2;0\rangle + B_n\langle (s_{1/2})^2;0||M_0^C||(s_{1/2})^2;0\rangle + C_n\langle \Psi_0||M_0^C||\Psi_0\rangle ,$$

where $M_L^C(q)$ is the 2^L-pole Coulomb transition operator, q is the momentum transfer, and the coefficients A_n, B_n, and C_n are computed[28] from the expansion coefficients of the states involved. The measurement of the electron-scattering form factors for the three 0^+ states in ^{18}O that are described by the model determines (if the signs of these matrix elements can be established) the three basic matrix elements. From these one can determine the momentum distribution (or equivalently, the spatial

distribution) of each basis state. It should be noted that each of these matrix elements describes the "pseudoelastic" scattering from a complete basis state; that is, from the core as well as from the valence nucleons.

For a quadrupole ($C2$) transition, the matrix element can be expressed as

$$\langle 2_n^+||M_2^C||0_1^+\rangle = D_n\langle d||M_2^C||d\rangle + E_n\langle s||M_2^C||d\rangle + F_n\langle \Psi_2||M_2^C||\Psi_0\rangle ,$$

where the states $|d\rangle$ and $|s\rangle$ are functions of the spatial coordinates only. One can obtain the momentum dependence of each matrix element by measuring the electon-scattering form factors for the lowest three 2^+ states in ^{18}O.

For a hexadecapole ($C4$) transition, the matrix element can be reduced to

$$\langle 4_n^+||M_4^C||0_1^+\rangle = G_n\langle d||M_4^C||d\rangle + H_n\langle \Psi_0||M_4^C||\Psi_0\rangle .$$

Since there are only two terms in this expression, the measurement of two 4^+ form factors suffices to determine the basic matrix elements.

By inverting the above relationships one can express the matrix elements involving the distinct components as functions of the measured form factors. The uncertainties assigned to the component matrix elements then can be computed from the uncertainties in the measured form factors.

Two points regarding this procedure warrant notice. First, by measuring a cross section one determines only the square of the corresponding matrix element; the sign of the matrix element is not determined. A second problem stems from the fact that when electrons of incident energy E_0 excite the nucleus to energies ω_1 and ω_2 by scattering through an angle θ, the momentum transfers involved are different [see Eq. (2)]. This problem was dealt with by choosing (for each E_0 and θ) the momentum transfer associated with the lowest-energy state of the multipolarity involved (i.e., 0_1^+, 2_1^+, and 4_1^+) as the standard. Then, from a graph containing all of the data for a subsequent level a value of the form factor for this level at the standard q was obtained by interpolation from the nearest data points. It should be noted that this interpolation does not involve any smoothing of the data. Other nearby data points were used only to determine the slope used in a linear interpolation.

Consider the 0^+ states. Since there are three measured form factors, there are four possible choices of signs ($+++$, $++-$, $+-+$, and $+--$). We assume that the difference between the radii of the 2p0h $(d_{5/2})^2$ component and the 2p0h $(s_{1/2})^2$ component is small compared to the difference between the radius of either of them and that of the deformed component. This assumption, along with the expansion coefficients of LSF, determines that at low momentum transfer the sign of the 0_3^+ form factor must be opposite that of the 0_2^+ form factor. This still leaves two choices ($+-+$ and $++-$). A decomposition was performed using each choice. First, the phase set ($+-+$) was assumed and the form factor for the pseudoelastic scattering from each component in the 0^+ wave functions was extracted. These extracted form factors then were subjected to FBA. The charge density of the collective deformed component was found to have a root-mean-square (rms) radius of 2.38 fm, much smaller than the 2.72-fm rms radius of ^{16}O.[18] The shape of the extracted charge density differs dramatically from that of ^{16}O; the central density is depressed and the surface severely sharpened. The d^2 (plus the spherical core) and s^2 (plus the spherical core) components have radii of 2.83 and 2.75 fm, respectively. When the valence neutrons are in the $d_{5/2}$ shell, charge is pulled from the region around 1.6 fm and moved outward, whereas when they are in the $s_{1/2}$ shell, charge is pulled outward from the center of the nucleus.

When the other phase set ($++-$) was assumed, it was impossible to trace the form factor of the collective deformed component through the diffraction minimum. Cancellations between various components cause the collective form factor to be determined by the difference of two relatively large numbers, and large fluctuations in the form factor result. It is, however, possible to trace the other two components because they are less sensitive to this problem. These extracted form factors are shown in Fig. 13. Above a momentum transfer of 1.3 fm^{-1}, the form factor of the collective state is not well enough determined to be of any use in the subsequent analysis. Only those values that are shown were used. The solid curves represent FBA fits to the extracted form factors.

The rms radii extracted for the various components are the following: d^2—2.74 fm, s^2—2.84 fm, and collective—3.18 fm. As before, the central density of the collective state is depressed, but now the surface is very diffuse (which explains the large rms radius). The differences between the charge densities of the d^2 and s^2 configurations and that of

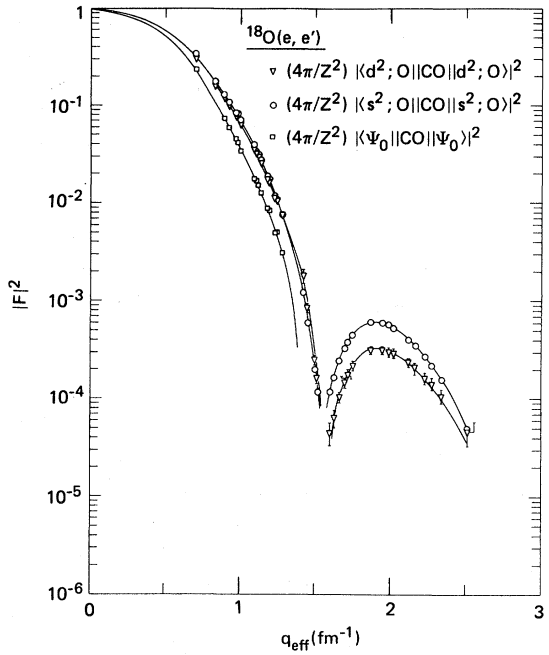

FIG. 13. Pseudoelastic form factors for the 0^+ basis states of the LSF model of ^{18}O. The solid curves represent FBA fits to the form factors.

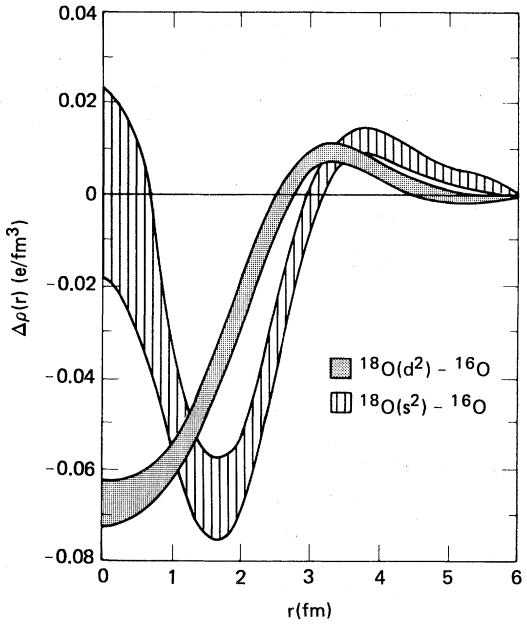

FIG. 14. Differences between the charge distributions of the two-neutron 0^+ basis states of the LSF model of ^{18}O and that of the ^{16}O ground state. The shaded (hatched) region shows the charge-distribution difference between the closed-shell-plus-d^2 (s^2) state and the ^{16}O ground state which contains a small nonspherical component.

^{16}O are shown in Fig. 14. They are similar to those obtained assuming the other phase set $(+\ -\ +)$, except that the roles of the configurations are reversed. In the present case, neutrons in the $d_{5/2}$ shell pull charge from the center of the nucleus while neutrons in the $s_{1/2}$ shell pull it from around 1.6 fm.

A treatment of the collective deformed component of ^{16}O as a triaxial rotor[44] yields the result that the deformed component has a larger radius and larger diffuseness than the spherical component. The phase set $(+\ +\ -)$ yields the same relative results and is, therefore, more appealing. The collective state in that calculation has an rms radius of 3.07 fm, very close to the radius of the collective state in ^{18}O.

The differences between the charge densities of the 2p0h configurations in ^{18}O and the charge density of ^{16}O also favor this choice of phase set. The major lobe of a $1s$ wave function occurs at a larger radius than does that of a $0d$ wave function. Therefore, one would expect that a particle in the $1s$ shell would pull charge out a larger radius. Such is the case when the phase set $(+\ +\ -)$ is assumed.

It should be noted that these comparisons are to the physical ^{16}O charge distribution, which itself contains not only a spherical component but also a deformed component. The contribution of this deformed component is small (about 10%).[11] To a similar level of accuracy one can view the ground state of ^{17}O as a $0d_{5/2}$ neutron coupled to ^{16}O. Within the context of this picture one would expect the difference between the charge distributions of ^{17}O and ^{16}O to be similar to one half the difference between the charge distribution of the d^2 (spherical core plus two $0d_{5/2}$ neutrons) components of ^{18}O and that of ^{16}O. Figure 15 shows these differences; the ^{18}O(d^2)$-^{16}$O charge-distribution difference is that determined assuming the phase set $(+\ +\ -)$ and the ^{17}O$-^{16}$O charge-distribution difference is from Ref. 18 (Appendix C). In view of the similarities between these charge-distribution differences it is not surprising that the rms radius computed for ^{17}O from the ^{18}O results

$$r(^{17}\mathrm{O}) = r(^{16}\mathrm{O}) + \{ r[^{18}\mathrm{O}(d^2)] - r(^{16}\mathrm{O}) \}/2$$
$$= 2.73 \text{ fm}$$

is in close agreement with the observed rms radius for ^{17}O of 2.71 ± 0.01 fm.[18] These results indicate that the analysis using the phase set $(+\ +\ -)$ yields a physically reasonable and consistent pic-

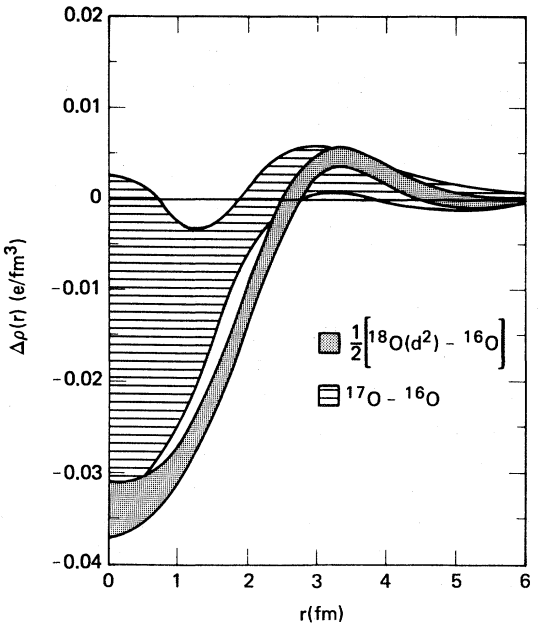

FIG. 15. Charge-distribution differences between ^{17}O and ^{16}O. The shaded region shows the charge-distribution difference computed from the results of the ^{18}O decomposition (see text). The hatched region shows the observed charge-distribution difference.

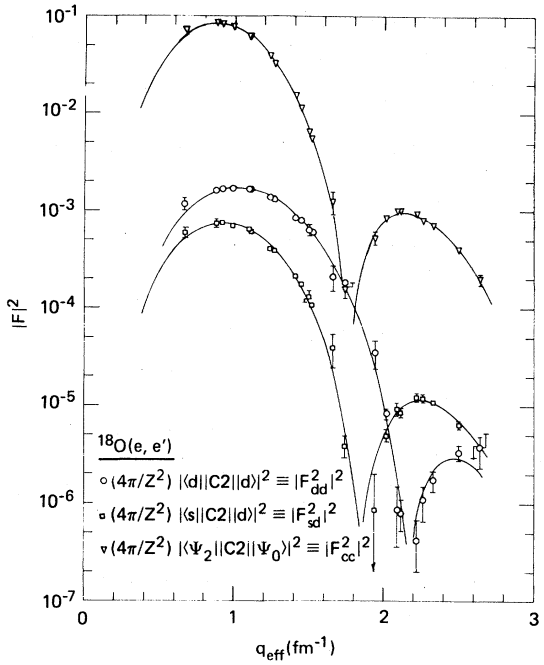

FIG. 16. Form factors for quadrupole transitions between basis states of the LSF model of ^{18}O. The solid curves represent FBA fits to the form factors.

ture.

Throughout the above analysis the parameters from the "unconstrained" fit of LSF were used. Little difference was seen between results obtained using this set and results obtained using a different set.

The choice of phase set for the decomposition of the 2^+ form factors is much easier. Only one choice yields matrix elements whose signs are consistent with those obtained by LSF. The form factors for the components of the 2^+ transitions are shown in Fig. 16.

It is interesting to compare the longitudinal part of the transition to the first excited state of ^{17}O ($\frac{1}{2}^+$, 0.871 MeV) to a d-to-s single particle Coulomb transition which should have a form factor similar to that obtained for a d-to-s transition in ^{18}O. The solid curve in Fig. 17 is computed (under the assumption that the transition is purely $0d_{5/2}$ to $1s_{1/2}$) from the d-to-s form factor extracted from the ^{18}O data. The fact that the curve falls below the data implies that collective configurations may be playing a role. The collective-collective (C-C) $C2$ form factor has the same shape as the d-to-s single-particle form factor so the inclusion of such a component into the description of the Coulomb transition to the first excited $\frac{1}{2}^+$ state of ^{17}O would sim-

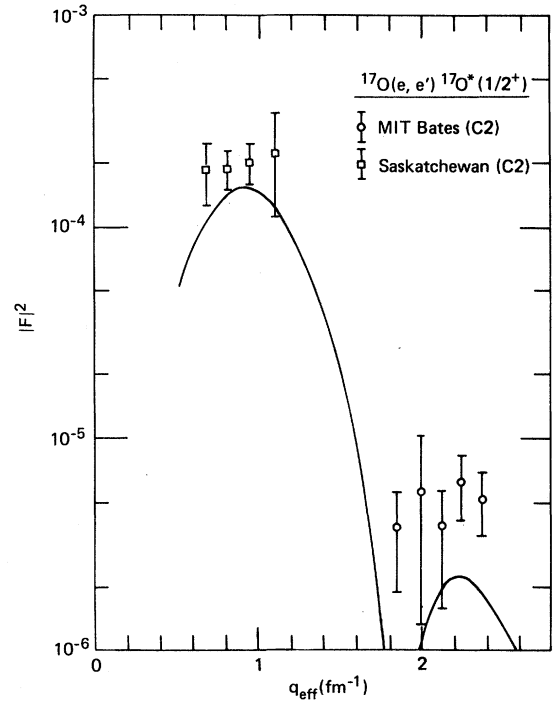

FIG. 17. Form factor for the longitudinal quadrupole excitation of the first $\frac{1}{2}^+$ (0.871 MeV) state in ^{17}O. The circles are from the present work and the squares are from Ref. 45. The solid curve is computed from the d-to-s quadrupole transition matrix element deduced from the form factors of the low-lying 2^+ states in ^{18}O.

ply scale upwards the curve shown in Fig. 17; e.g., the inclusion of a 5% *C-C C2* component in this transition would scale this curve upwards by 40% and thus would result in a good fit to the data. Such a contribution would be consistent with the known[46] spectroscopic factors of the ground and first excited states of ^{17}O [$S(\frac{5}{2}^+) \approx S(\frac{1}{2}^+) \approx 0.9$].

Another important comparison is between the *C-C C2* transition in ^{18}O and the 0_1^+-to-2_1^+ transition in ^{16}O. The solid curve in Fig. 18 represents the *C-C C2* form factor scaled to fit the measured $B(E2)$ for the transition in ^{16}O. The agreement is striking. The shape of the form factor and the location of its diffraction minimum are reproduced precisely. Even the magnitude and shape of the second lobe are not inconsistent with the data. This agreement is not a trivial consequence of fitting parameters to reproduce $B(E2)$ values; the momentum-transfer dependences of the three measured form factors that contribute to the determination of this form factor are significantly different (see Figs. 5—7, and Table II). Furthermore, only one ground-state $B(E2)$ value ($2_1^+ \rightarrow 0_1^+$) was involved in the LSF fit. The agreement, therefore, is strong evidence that the collective states in ^{16}O and ^{18}O have very similar structures.

If one assumes that the 2_1^+ state in ^{16}O is purely deformed, then it can be argued[11] that the contribution of the deformed component to the ground state of ^{16}O is about 10%. If one also assumes that the collective deformed configurations in ^{16}O are identical to those in ^{18}O, then the form factor of the 2_1^+ excitation in ^{16}O is computed to be too large by a factor of 2.5. This indicates that the deformed component of ^{16}O is more complex than assumed.

The 2^+ component form factors were subjected to FBA and the resulting fits are shown by the solid curves in Fig. 16. The extracted transition charge densities are shown in Fig. 19. The *d*-to-*d* transition density is seen to be everywhere positive, to be about 2.3 fm wide at half maximum, and to peak at 2.3 fm. The transition density for a single-particle *d*-to-*d* transition computed using Woods-Saxon wave functions with parameters taken from Donnelly and Walker[48] (radius 3.25 fm, diffuseness 0.5 fm, spin-orbit strength 6 MeV, and well depth 50.6 MeV) shows the same behavior. It peaks at a radius of 2.3 fm, is 2.3 fm wide at half its maximum value, and is everywhere positive. on the other hand, the extracted *d*-to-*s* transition density is seen to peak at

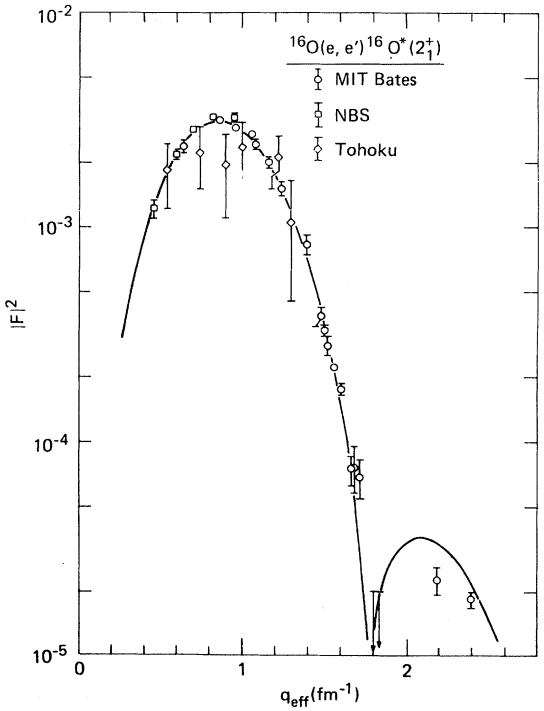

FIG. 18. Form factor for the excitation of the first 2^+ (6.917 MeV) state in ^{16}O. The circles are from the present work, the squares are from Ref. 44, and the diamonds are from Ref. 47. The solid curve is the collective-collective quadrupole-transition matrix element deduced from the form factors of the low-lying 2^+ states in ^{18}O scaled to reproduce the $B(E2)$ for the $0_1^+ \rightarrow 2_1^+$ transition in ^{16}O.

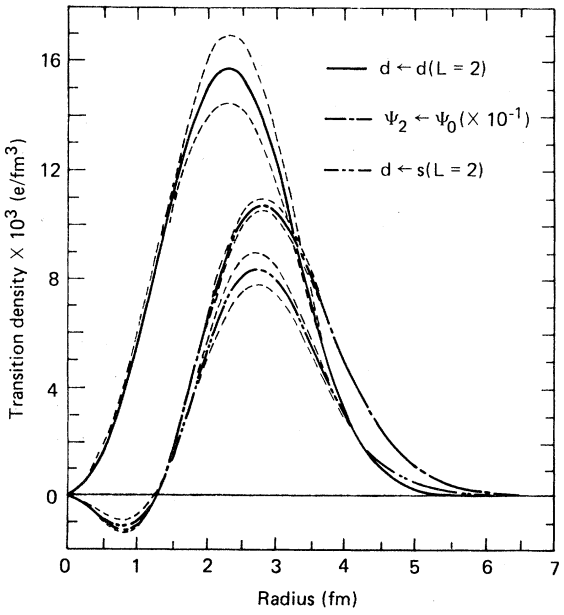

FIG. 19. Transition charge densities for quadrupole transition between basis states of the LSF model of ^{18}O.

2.8 fm and to have a small negative lobe near the origin. A calculation for a *d*-to-*s* transition using the above potential well yields a transition density which also peaks at 2.8 fm, but has a large negative lobe near the origin. That the extracted *d*-to-*s* transition density has a more shallow inner lobe is not surprising. The polarization effects which generate the charge density are collective in nature and therefore are predominantly surface effects.

The 4^+ form factors can be expanded in terms of two components only; that corresponding to a *d*-to-*d* transition and that corresponding to a *C*-*C* transition. By measuring the form factors of the lowest two 4^+ states one can determine these components and then use them to predict the form factor of the third 4^+ state. Again, an assumption for the relative phase between the two measured form factors must be made. In the present case the choice is made so that the form factor of the collective (*C*-*C*) transition is larger than that of the single-particle transition. The resulting decomposition of the form factors into their LSF components is shown in Fig. 20. Here, the choice of the LSF parameter set had a measurable effect on the form factors that were extracted. The circles in Fig. 20 show the results obtained for the *C*-*C* form factor when the "constrained II" parameters of LSF were used, while the squares show the corresponding results obtained with their "unconstrained" parameters. For the subsequent steps in the analysis, the form factors obtained using the unconstrained parameters were used.

The solid curves in Fig. 20 represent the FBA fits to these components. The prediction of the model for the form factor of the third 4^+ state is shown by the shaded band in Fig. 8. The agreement up to the maximum of the form factor is excellent, giving strong indication that the state at 7.848 MeV is indeed the third 4^+ state. However, beyond the maximum there is pronounced disagreement. The source of this discrepancy is not clear. It is possible that the model simply is not adequate to describe the high-momentum components of these excitations. It also is possible that an unresolved state of multipolarity greater than 4 exists near the 7.848-MeV level.

The transition charge distributions for the LSF components of the 4^+ states are shown in Fig. 21. The shapes of the transition charge densities for the two physical 4^+ transitions are very similar in shape (see Fig. 12), so it is no surprise that the charge densities for the components of these transitions are very similar in shape as well.

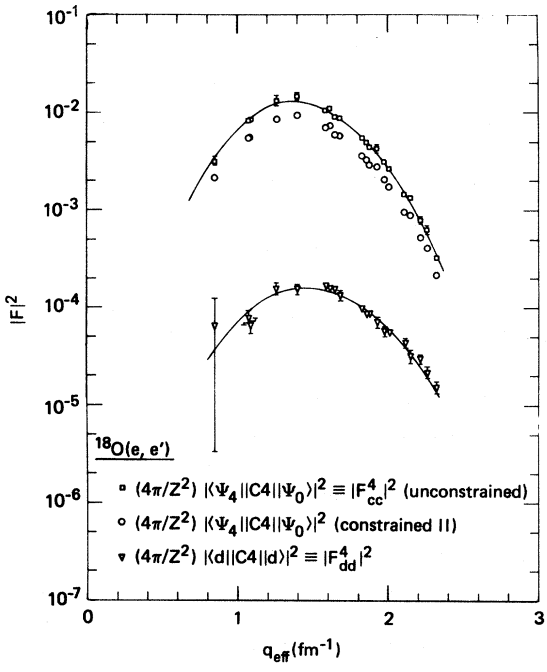

FIG. 20. Form factors for hexadecapole transitions between basis states of the LSF model of ^{18}O. The labels in parentheses denote the set of constraints applied in computing the wave functions (see Ref. 11). The solid curves represent FBA fits to the form factors.

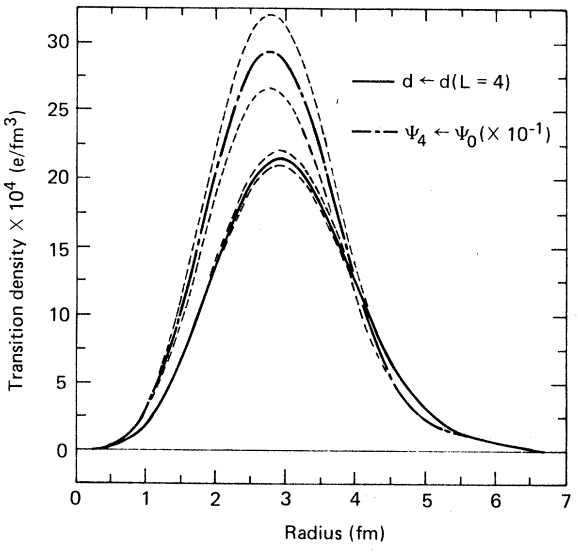

FIG. 21. Transition charge densities for hexadecapole transitions between basis states of the LSF model of ^{18}O.

V. SUMMARY AND CONCLUSIONS

We have measured the inelastic electron-scattering form factors for eight low-lying even-parity states in ^{18}O in the range of momentum transfer from 0.6 to 2.7 fm^{-1}. Data obtained at two angles show that these form factors have no appreciable transverse components. Fourier-Bessel analyses were performed to yield transition charge densities and $B(EL)$ values.

The measured form factors were compared with the predictions of various theoretical models, but in no case did the calculated results represent a good fit to the data. In addition, the measured form factors were decomposed into single-particle and collective components within the context of the coexistence model of Lawson, Serduke, and Fortune. From these components we have extracted single-particle and collective transition charge densities which represent a physically reasonable picture of ^{18}O. These densities have shapes which are appropriate for corresponding transitions in ^{16}O and ^{17}O. It would be very interesting to see this calculation refined by the inclusion of the present data.

The experimental results presented here underscore the need for additional experimental and theoretical effort. More and better measurements of the 0_3^+ and 4_3^+ form factors of ^{18}O should be made, and it is at least equally important that better data on the low-lying levels of both ^{16}O and ^{17}O be obtained. The availability of such data would enable one to obtain a much improved picture of the similarities among the oxygen isotopes. An experimental program to obtain these data is in progress.

ACKNOWLEDGMENTS

We gratefully acknowledge the assistance and support of our colleagues. In particular, we wish to thank J. Heisenberg for many useful discussions and much valuable advice. We also wish to thank I. Morrison, P. J. Ellis, and J. B. McGrory for providing us with the results of their calculations. This research was performed at the MIT-Bates Linear Accelerator Laboratory and was supported in part by the U. S. Department of Energy, under Contract No. EY-76-C-02-3069.*000, the National Research Council of Canada, and the Deutscher Akademischer Austausch Dienst.

APPENDIX A: MEASURED FORM FACTORS

The form factors are defined by

$$|F(q)|^2=\frac{d\sigma}{d\Omega}\Big/Z^2\sigma_M\eta\ ,$$

where

$$\sigma_M=[(\alpha/2E_0)^2\cos^2(\theta/2)/\sin^4(\theta/2)]$$

is the Mott cross section,

$$\eta=[1+(2E_0/M)\sin^2(\theta/2)]^{-1}$$

is the recoil factor, Z is the atomic number of the target nucleus, E_0 is the incident electron energy, θ is the scattering angle, α is the fine-structure constant, and M is the mass of the target nucleus.

The second column of each table (see Tables IV–VIII) contains the effective momentum transfer for elastic scattering. It is defined by

$$q_{\rm eff}^{\rm el}=2E_0\sin(\theta/2)\eta^{1/2}\times\left[1+\frac{3}{2}\left[\frac{3}{5}\right]^{1/2}\frac{Z\alpha}{E_0\langle r^2\rangle^{1/2}}\right],$$

where $\langle r^2\rangle^{1/2}$ is the rms radius of ^{18}O (2.794 fm). This momentum transfer is related to the effective momentum transfer for inelastic scattering to each of the excited states by

$$q_{\rm eff}^{\rm inel}=q_{\rm eff}^{\rm el}\sqrt{1-\omega/E_0}\ ,$$

where ω is the energy of the excited state. The notation for the form factors is such that

$$a.bc(-d)=a.bc\times10^{-d}\ .$$

The uncertainty quoted for each form factor includes systematic as well as statistical uncertainties.

APPENDIX B: TARGET-COMPOSITION ANALYSIS

The relative abundances of the oxygen isotopes in the mixed-isotope targets were determined by examining elastic-scattering data ($E_0=165.0$ MeV, $\theta=90°$; see Fig. 3) from the complete set of targets (see Table I). A target made from naturally occurring oxygen (Be^{16}O) also was used.

Data from two isotopically-mixed targets were used in conjunction with data from the Be^{16}O target. From the data gathered using the Be^{16}O target elastic cross sections for ^{16}O (σ_{16}) and for ^{9}Be (σ_9) were extracted. From each of the other two targets the Be cross section and the products of the individual oxygen-isotope cross sections (σ_n^m) and the corresponding abundances (η_n^m) were extracted (the m denotes the target used for the measurement and n denotes the isotope). The overall accuracy of these measurements is limited by uncertainties in (1) the beam-current monitoring, (2) the target thicknesses and uniformities, and (3) the dead-time corrections. These uncertainties were removed by

TABLE IV. Form factors for 0^+ states measured at 90°.

E_0 (MeV)	q_{eff} (fm^{-1})	$\|F(0_2^+)\|^2$ (3.63 MeV)	Error (%)	$\|F(0_3^+)\|^2$ (5.33 MeV)	Error (%)
90.29	0.676	5.14(−4)	10	<5.00(−5)	
111.65	0.826	5.60(−4)	4		
120.46	0.888	4.97(−4)	10	2.00(−5)	60
125.65	0.925	4.10(−4)	4		
131.49	0.965	3.65(−4)	5		
132.59	0.973	3.91(−4)	5		
135.50	0.993	4.15(−4)	15	2.00(−5)	70
148.26	1.082	2.55(−4)	4	3.05(−5)	30
150.54	1.098	1.95(−4)	5		
152.20	1.110	2.05(−4)	3	1.68(−5)	30
154.92	1.129	1.79(−4)	5	<6.00(−5)	
161.22	1.172	1.19(−4)	4		
162.46	1.181	1.04(−4)	5	2.00(−5)	50
168.22	1.222	8.42(−5)	5		
170.42	1.237	5.61(−5)	10		
175.16	1.269	5.09(−5)	8	2.00(−5)	80
194.41	1.403	<1.60(−6)			
199.90	1.441	5.00(−6)	20		
207.06	1.491	1.07(−5)	30		
209.85	1.510	1.18(−5)	10		
213.11	1.532	1.56(−5)	17		
221.05	1.588	2.85(−5)	10		
224.70	1.612	3.69(−5)	7		
229.59	1.646	4.30(−5)	4		
234.25	1.678	4.99(−5)	6		
236.80	1.695	5.50(−5)	8	<1.00(−5)	
241.18	1.726	5.64(−5)	6	<4.00(−6)	
258.83	1.847	6.28(−5)	4		
261.92	1.867	6.18(−5)	6		
269.50	1.920	6.19(−5)	8	<4.00(−6)	
275.26	1.959	6.31(−5)	5		
280.43	1.994	5.44(−5)	4	2.00(−6)	80
291.14	2.067	4.72(−5)	12	<4.00(−6)	
294.35	2.089	4.12(−5)	4		
300.54	2.131	3.47(−5)	8	<4.00(−6)	
309.57	2.192	2.96(−5)	5		
315.80	2.234	2.16(−5)	6	<4.00(−6)	
325.09	2.297	1.70(−5)	5		
349.25	2.461	5.87(−6)	9		

normalizing the oxygen cross sections to that of beryllium as measured during the same exposure

$$(\Sigma_n^m=\eta_n^m\sigma_n^m/\sigma_9^m=\eta_n^m\Sigma_n)\ .$$

This was possible because the oxygen and beryllium atoms are known to exist in a one-to-one ratio in each target.

The data from the three targets can be reduced to seven independent quantities:

$$\Sigma_{16}{}^1=0.998\sigma_{16}{}^1/\sigma_9{}^1=0.998\Sigma_{16}\ ,$$

$$\Sigma_{16}{}^2=\eta_{16}{}^2\Sigma_{16}\ ,\quad \Sigma_{17}{}^2=\eta_{17}{}^2\Sigma_{17}\ ,\quad \Sigma_{18}{}^2=\eta_{18}{}^2\Sigma_{18}\ ,$$

$$\Sigma_{16}{}^3=\eta_{16}{}^3\Sigma_{16}\ ,\quad \Sigma_{17}{}^3=\eta_{17}{}^3\Sigma_{17}\ ,\quad \Sigma_{18}{}^3=\eta_{18}{}^3\Sigma_{18}\ .$$

TABLE V. Form factors for 2^+ states measured at 90°.

E_0 (MeV)	q_{eff} (fm^{-1})	$\lvert F(2_1^+)\rvert^2$ (1.98 MeV)	Error (%)	$\lvert F(2_2^+)\rvert^2$ (3.92 MeV)	Error (%)	$\lvert F(2_3^+)\rvert^2$ (5.25 MeV)	Error (%)
90.29	0.676	2.96(−3)	7	1.12(−3)	8	1.50(−3)	7
91.35	0.683	2.84(−3)	4				
111.65	0.826	3.74(−3)	2	1.40(−3)	3		
120.46	0.888	3.74(−3)	3	1.31(−3)	6	1.79(−3)	7
125.65	0.925	3.76(−3)	3	1.25(−3)	3	1.74(−3)	3
131.49	0.965	3.78(−3)	2	1.17(−3)	3		
132.59	0.973	3.98(−3)	3				
135.50	0.993	3.58(−3)	3	1.13(−3)	4	1.63(−3)	4
148.26	1.082	3.36(−3)	2			1.37(−3)	2
150.54	1.098	3.25(−3)	2	8.87(−4)	6	1.26(−3)	5
152.20	1.110	3.24(−3)	2	8.80(−4)	2	1.31(−3)	2
154.92	1.129	3.22(−3)	2			1.27(−3)	3
161.22	1.172	2.74(−3)	2			9.86(−4)	3
162.46	1.181	2.66(−3)	3			9.28(−4)	3
165.08	1.200	2.53(−3)	2	6.00(−4)	4		
168.22	1.222	2.37(−3)	4	4.96(−4)	4	8.71(−4)	5
170.42	1.237	2.28(−3)	3	4.78(−4)	6	8.37(−4)	4
175.16	1.269	2.09(−3)	3	3.96(−4)	5	6.68(−4)	5
185.75	1.344			2.12(−4)	6	4.40(−4)	5
194.41	1.403	1.17(−3)	4	1.56(−4)	7	2.96(−4)	6
199.90	1.441	1.01(−3)	2	9.75(−5)	7	2.11(−4)	5
207.06	1.491	7.29(−4)	11	4.97(−5)	11	1.10(−4)	12
209.85	1.510	6.50(−4)	4	3.30(−5)	9	9.64(−5)	10
213.11	1.532			2.18(−5)	14	8.55(−5)	15
221.05	1.588	3.77(−4)	3	6.55(−6)	30		
224.70	1.612	2.84(−4)	4	2.00(−6)	45		
229.59	1.646	2.09(−4)	3			1.55(−5)	24
234.25	1.678	1.52(−4)	4				
236.80	1.695	1.24(−4)	6				
241.18	1.726	9.17(−5)	5	7.38(−6)	11	4.12(−6)	35
254.69	1.818	1.91(−5)	4	2.16(−5)	6		
258.83	1.847	1.06(−5)	7				
261.92	1.867	6.91(−6)	9			6.30(−6)	32
269.50	1.920	8.50(−7)	100	3.32(−5)	9	1.29(−5)	18
275.26	1.959			3.81(−5)	5		
280.43	1.994	4.08(−6)	11	3.75(−5)	5	1.74(−5)	9
291.14	2.067	1.44(−5)	11	3.83(−5)	7	1.89(−5)	15
294.35	2.089	1.39(−5)	4	3.69(−5)	5	1.93(−5)	8
300.54	2.131	1.80(−5)	10				
309.57	2.192	2.34(−5)	4	3.24(−5)	5	1.50(−5)	12
315.80	2.343	2.35(−5)	6	2.76(−5)	5	1.24(−5)	10
325.09	2.297	2.29(−5)	4	2.37(−5)	5	1.11(−5)	6
349.25	2.461	1.67(−5)	5	1.12(−5)	8	6.18(−6)	8
369.16	2.594	1.12(−5)	20	4.83(−6)	15	2.78(−6)	25

Furthermore,

$$\eta_{16}^2+\eta_{17}^2+\eta_{18}^2=1\ ,$$

$$\eta_{16}^3+\eta_{17}^3+\eta_{18}^3=1\ .$$

Thus, the problem is completely determined. Solving for the desired η_n^m's yields:

$$\eta_{16}^2=\Sigma_{16}^2/\Sigma_{16}\ ,\quad \eta_{16}^3=\Sigma_{16}^3/\Sigma_{16}\ ,$$

$$\eta_{17}^2=\frac{(1-\eta_{16}^3)\Sigma_{17}^2/\Sigma_{17}^3-(1-\eta_{16}^2)\Sigma_{18}^3/\Sigma_{18}^2}{1-\Sigma_{18}^3/\Sigma_{18}^2}\ ,$$

TABLE VI. Form factors for 4^+ states measured at 90°.

E_0 (MeV)	q_{eff} (fm^{-1})	$\|F(4_1^+)\|^2$ (3.55 MeV)	Error (%)	$\|F(4_2^+)\|^2$ (7.11 meV)	Error (%)	$\|F(4_3^+)\|^2$ (7.85 MeV)	Error (%)
120.46	0.888			1.70(−4)	11		
135.50	0.993			2.94(−4)	7	1.35(−5)	80
148.26	1.082	3.55(−5)	13	4.33(−4)	3		
150.54	1.098	3.10(−5)	14	4.35(−4)	5	3.60(−5)	20
152.20	1.110	4.30(−5)	8				
154.92	1.129	3.90(−5)	18				
161.22	1.172	4.30(−5)	8				
162.46	1.181			5.16(−4)	5	5.61(−5)	15
165.08	1.200	5.29(−5)	8				
168.22	1.222	5.67(−5)	7				
175.16	1.269	6.80(−5)	10	7.00(−4)	10	4.38(−5)	20
185.75	1.344	7.00(−5)	15				
194.41	1.403	6.92(−5)	7	7.81(−4)	6		
199.90	1.441	8.04(−5)	5				
207.06	1.491	7.28(−5)	11			4.10(−5)	20
209.85	1.510	7.24(−5)	10				
213.11	1.532	5.90(−5)	14	5.23(−4)	14	3.52(−5)	25
221.05	1.588	6.93(−5)	6	6.06(−4)	4	5.72(−5)	10
224.70	1.612	6.57(−5)	5	6.32(−4)	5		
229.59	1.646	6.28(−5)	4	5.24(−4)	3	5.29(−5)	6
234.25	1.678	5.50(−5)	6	5.02(−4)	5	7.00(−5)	20
236.80	1.695	5.56(−5)	8			6.70(−5)	10
241.18	1.726	5.41(−5)	6			6.79(−5)	7
254.69	1.818	3.95(−5)	4	3.20(−4)	3		
258.83	1.847	3.46(−5)	4	2.86(−4)	3	5.91(−5)	10
261.92	1.867	3.43(−5)	7	2.58(−4)	5	6.31(−5)	13
269.50	1.920	2.88(−5)	9	2.48(−4)	8	5.00(−5)	20
275.26	1.959	2.30(−5)	8	1.86(−4)	3	4.74(−5)	10
280.43	1.994	2.16(−5)	6	1.60(−4)	7	3.61(−5)	6
291.14	2.067	1.62(−5)	23			3.67(−5)	8
294.35	2.089	1.60(−5)	6	9.11(−5)	4		
300.54	2.131	1.22(−5)	14	8.24(−5)	6	3.06(−5)	14
309.57	2.192	1.07(−5)	8	5.14(−5)	5		
315.80	2.234	7.85(−6)	11	3.94(−5)	5	2.10(−5)	20
325.09	2.297	5.35(−6)	11	2.16(−5)	5	2.10(−5)	25
349.25	2.461	2.60(−6)	26				
369.16	2.594	<1.00(−6)					

TABLE VII. Form factors for 0_2^+ and 4^+ states measured at 160°.

E_0 (MeV)	q_{eff} (fm^{-1})	$\|F(4_1^+)\|^2$ (3.55 MeV)	Error (%)	$\|F(0_2^+)\|^2$ (3.63 MeV)	Error (%)	$\|F(4_2^+)\|^2$ (7.11 MeV)	Error (%)
125.58	1.278	6.50(−5)	24	6.40(−5)	30		
133.78	1.357	7.46(−5)	25				
142.39	1.440	9.03(−5)	13				
151.34	1.527	7.20(−5)	20			5.33(−4)	14
171.22	1.717					3.17(−4)	13
208.59	2.074	1.87(−5)	84	6.29(−5)	27		
234.18	2.317	9.00(−5)	35	1.29(−5)	38		
245.23	2.422					<2.00(−5)	

TABLE VIII. Form factors for 2^+ states measured at 160°.

E_0 (MeV)	q_{eff} (fm^{-1})	$\lvert F(2_1^+)\rvert^2$ (1.98 MeV)	Error (%)	$\lvert F(2_2^+)\rvert^2$ (3.92 MeV)	Error (%)	$\lvert F(2_3^+)\rvert^2$ (5.25 MeV)	Error (%)
125.38	1.275	2.08(−3)	4				
125.58	1.278	2.17(−3)	14	4.45(−4)	14		
133.78	1.313			2.56(−4)	20		
142.39	1.440	9.15(−4)	5				
151.34	1.527	5.60(−4)	7	1.48(−5)	35		
208.59	2.074	1.33(−5)	33	3.90(−5)	15		
234.18	2.317	3.05(−5)	15	2.76(−5)	22	9.59(−6)	38
245.23	2.422	2.30(−5)	16				
255.00	2.513	2.02(−5)	27				
256.23	2.525	2.17(−5)	20				
275.23	2.703	8.50(−6)	57				

$$\eta_{18}{}^2=\frac{(1-\eta_{16}{}^3)\Sigma_{18}{}^2/\Sigma_{18}{}^3-(1-\eta_{16}{}^2)\Sigma_{17}{}^3/\Sigma_{17}{}^2}{1-\Sigma_{17}{}^3/\Sigma_{17}{}^2},$$

$$\eta_{17}{}^3=\frac{(1-\eta_{16}{}^2)\Sigma_{17}{}^3/\Sigma_{17}{}^2-(1-\eta_{16}{}^3)\Sigma_{18}{}^2/\Sigma_{18}{}^3}{1-\Sigma_{18}{}^2/\Sigma_{18}{}^3},$$

$$\eta_{18}{}^3=\frac{(1-\eta_{16}{}^2)\Sigma_{18}{}^3/\Sigma_{18}{}^2-(1-\eta_{16}{}^3)\Sigma_{17}{}^2/\Sigma_{17}{}^3}{1-\Sigma_{17}{}^2/\Sigma_{17}{}^3},$$

where each η_n^m is a function of seven statistically independent measurements. The uncertainty in each η_n^m was computed by adding in quadrature the changes that resulted from a change of one standard deviation in each Σ_n^m.

It may be noted that the use of the $Be^{16}O$ target was not strictly necessary. Any set of three beryllium-oxide targets with differing isotopic compositions could have been used. However, the use of one well understood target helped to reduce the uncertainties in the extracted abundances.

APPENDIX C: GROUND STATE CHARGE DENSITIES

Following Ref. 37, a ground state charge density is represented by

TABLE IX. Ground state charge density parameters.

Nucleus Coefficient	n	^{16}O C_n (fm^{-2})$\times 10^3$	^{17}O C_n (fm^{-2})$\times 10^3$	^{18}O C_n (fm^{-2})$\times 10^3$
	1	1.80±0.66	0.92±0.78	−14.33±0.38
	2	2.04±1.30	−3.63±1.20	−46.84±0.69
	3	−0.99±0.44	−9.39±0.74	−26.17±0.33
	4	−4.14±0.53	−1.58±0.74	9.46±0.43
	5	−15.56±0.40	−0.01±1.20	13.94±0.49
	6	−13.06±0.21		4.75±1.40
	8	−3.85±0.27		
R (fm)		6.0	6.5	6.5
ρ_0	$3pF$	$\rho_N=1.039$ fm^{-3} $C=2.608$ fm $Z=0.513$ fm $W=-0.051$	^{16}O (Col. 1)	^{16}O (Col. 1)

TABLE X. ^{18}O transition charge density parameters.

Excitation Coefficient	n	2_1^+ (1.98 MeV) a_n (fm^{-3})$\times 10^3$	2_2^+ (3.92 MeV) a_n (fm^{-3})$\times 10^3$	2_3^+ (5.25 MeV) a_n (fm^{-3})$\times 10^3$	4_1^+ (3.55 MeV) a_n (fm^{-3})$\times 10^3$	4_2^+ (7.11 MeV) a_n (fm^{-3})$\times 10^3$
	1	9.809±0.266	6.324±0.448	7.265±0.266	1.334±0.168	4.610±0.242
	2	18.340±0.768	9.320±1.339	11.327±0.671	2.818±0.418	8.679±0.596
	3	10.014±0.228	1.782±0.073	3.538±0.149	2.273±0.160	6.002±0.182
	4	−0.668±0.031	−3.370±0.117	−2.063±0.109	0.999±0.083	1.686±0.088
	5	−2.883±0.085	−2.517±0.108	−1.751±0.087	0.508±0.116	0.171±0.217
	6	−1.127±0.246	−0.805±0.300	−0.589±0.221	0.390±0.107	0.339±0.152
	7	−0.276±0.321	−0.603±0.566	−0.283±0.251	0.062±0.109	0.019±0.145
	8	0.047±0.203	−0.060±0.510	0.049±0.164	−0.056±0.064	−0.016±0.076
	9	0.062±0.069	0.203±0.236	0.058±0.060	0.006±0.033	0.025±0.021
	10	0.016±0.048	0.004±0.179	0.012±0.050	−0.004±0.027	0.004±0.012
	11	0.004±0.037	−0.014±0.171	0.006±0.035	−0.001±0.021	−0.002±0.009
R (fm)		7.0	7.0	7.0	7.0	7.0

$$\rho(r)=\rho_0(r)+\sum_{n=1}^{N}\frac{C_n}{r}\sin\left[\frac{n\pi r}{R}\right];\quad r\le R$$

$$=\rho_0(r);\quad r>R\ ,$$

where $\rho_0(r)$ is an initial estimate of $\rho(r)$, and R is the radius beyond which is adequately described by $\rho_0(r)$. A common form for $\rho_0(r)$ is the three parameter Fermi ($3pF$) distribution

$$\rho_0(r)=\rho_N\frac{1+Wr^2/C^2}{\left[1+e^{\frac{r-C}{Z}}\right]}\ .$$

Table IX contains the parameters which describe the ground state charge densities of ^{16}O, ^{17}O (spherical component only), and ^{18}O. The errors quoted are statistical only.

APPENDIX D: TRANSITION CHARGE DENSITIES

Following Ref. 36, a 2^J-pole transition charge density is represented by

$$\rho_{\rm tr}^J(r)=\sum_{n=1}^{N}a_n X_n^{J-1} j_J(X_n^{J-1}r/R)\theta(R-r)\ ,$$

where X_n^{J-1} is the nth zero of the spherical Bessel function $j_{J-1}(x)$ and R is the radius beyond which $\rho_{\rm tr}(r)$ is assumed to be zero.

Table X contains the parameters which describe the charge densities associated with transitions from the ground state of ^{18}O to the lowest three 2^+ states (2_1^+—1.982 MeV, 2_2^+—3.919 MeV, 2_3^+—5.250 MeV), and the lowest two 4^+ states (4_1^+—3.553 MeV, 4_2^+—7.114 MeV). The uncertainties in these densities are shown by the error bands in Figs. 11 and 12.

*Present address: Department of Physics, University of Virginia, Charlottesville, Virginia 22901.
†Present address: Los Alamos National Laboratory, Los Alamos, New Mexico 87544.
‡Present address: Institut für Kernphysik, Universitat Mainz, Mainz, West Germany.
§Present address: Fermi National Accelerator Laboratory, Batavia, Illinois 60510.
||Present address: Laboratory of Nuclear Science, Tohoku University, Sendai, Japan.

[1]J. P. Elliot and B. H. Flowers, Proc. R. Soc. London Ser. A 229, 536 (1955).
[2]J. P. Elliot and B. H. Flowers, Proc. R. Soc. London Ser. A 242, 57 (1957).
[3]M. Redlich, Phys. Rev. 110, 468 (1958).
[4]T. Engeland and A. Kallio, Nucl. Phys. 59, 211 (1964).
[5]T. T. S. Kuo and G. E. Brown, Nucl. Phys. 85, 40 (1966).
[6]G. E. Brown, in *Proceedings of the International Congress on Nuclear Physics, Paris, 1964,* edited by P. Gugenburger (Centre National de la Recherche Scientifique, Paris, 1964), Vol. I, p. 129.

[8]W. H. Bassichis and G. Ripka, Phys. Lett. 15, 320 (1965).
[9]G. E. Brown and A. M. Green, Nucl. Phys. 75, 401 (1966); 85, 87 (1966).
[10]H. G. Benson and J. M. Irvine, Proc. R. Phys. Soc. 89, 249 (1966).
[11]R. D. Lawson *et al.*, Phys. Rev. C 14, 1245 (1976).
[12]I. Morrison *et al.*, Phys. Rev. C 17, 1485 (1978).
[13]P. J. Ellis and T. Engeland, Nucl. Phys. A144, 161 (1970).
[14]J. B. McGrory and B. H. Wildenthal, Phys. Rev. C 7, 974 (1973).
[15]F. Ajzenberg-Selove, Nucl. Phys. A190, 1 (1972).
[16]G. R. Bishop *et al.*, Nucl. Phys. 53, 366 (1963).
[17]J. L. Groh *et al.*, Can. J. Phys. 49, 2743 (1971).
[18]H. Miska *et al.*, Phys. Lett. 83B, 165 (1979).
[19]B. E. Norum *et al.*, Bull. Am. Phys. Soc. 23, 960 (1978).
[20]J. Kelly *et al.*, Los Alamos National Laboratory Report No. LA-8303C, 1980 (unpublished).
[21]T. de Forest and J. D. Walecka, Adv. Phys. 15, 1 (1966).
[22]J. M. Eisenberg and W. Greiner, *Excitation Mechanisms of the Nucleus* (North-Holland, Amsterdam, 1970).
[23]W. Bertozzi *et al.*, IEEE Trans. Nucl. Sci. Ns-14, 191 (1967).
[24]W. Bertozzi *et al.*, Nucl. Instrum. Methods 141, 457 (1977).
[25]W. Bertozzi *et al.*, Nucl. Instrum. Methods 162, 211 (1979).
[26]R. H. Condit *et al.* (unpublished).
[27]M. V. Hynes *et al.*, Phys. Rev. Lett. 42, 1444 (1979).
[28]B. E. Norum, Ph.D. thesis, Massachusetts Institute of Technology, 1979.
[29]I. Sick and J. S. McCarthy, Nucl. Phys. A150, 63 (1970).
[30]W. Schutz, Z. Phys. A 273, 69 (1975).
[31]P. R. Bevington, *Data Reduction and Error Analysis for the Physical Sciences* (McGraw-Hill, New York, 1969).
[32]J. C. Bergstrom, in Medium Energy Nuclear Physics with Electron Linear Accelerators—MIT, 1967 Summer Study, edited by W. Bertozzi and S. Kowalski, U. S. Atomic Energy Commission Technical Information Division Report No. TID-24667, 1967, p. 251.
[33]V. Horsfjord, Nucl. Phys. A253, 216 (1975).
[34]I. Morrison (private communication).
[35]H. T. Fortrune *et al.*, as quoted in Ref. 11.
[36]J. Heisenberg, in *Advances in Nuclear Physics*, edited by J. W. Negele and E. Vogt (Plenum, New York, 1981), Vol. 12.
[37]J. L. Friar and J. W. Negele, Nucl. Phys. A240, 331 (1975).
[38]C. Flaum *et al.*, Phys. Rev. Lett. 39, 446 (1977).
[39]P. B. Vold, Phys. Rev. Lett. 39, 325 (1977).
[40]A. P. Zuker *et al.*, Phys. Rev. Lett. 21, 39 (1968).
[41]V. Horsfjord, Nucl. Phys. A209, 493 (1973).
[42]M. Harvey and F. C. Khanna, Nucl. Phys. A155, 337 (1970).
[43]S. G. Nilsson, K. Dan. Vidensk. Selsk. Mat. Fys. Medd. 29, No. 1 (1955).
[44]J. C. Bergstrom, Ph.D. thesis, Massachusetts Institute of Technology, 1971.
[45]J. C. Kim *et al.*, Phys. Lett. 57B, 341 (1975).
[46]S. E. Darden *et al.*, Nucl. Phys. A208, 77 (1973).
[47]Y. Torizuka (private communication).
[48]T. W. Donnelly and G. E. Walker, Phys. Rev. Lett. 23, 1121 (1969).